Statistical analysis of dynamic behavior of continental shelf wave motions in the northern South China Sea

Junyi Li[1,2,3], Tao He[1,3], Quanan Zheng[1,4], Ying Xu[3], Lingling Xie[1*]

[1] Laboratory of Coastal Ocean Variation and Disaster Prediction, College of Ocean and Meteorology, Guangdong Ocean University, Zhanjiang 524088, China

[2] Key Laboratory of Climate, Sources and Environments in Continent Shelf Sea and Deep Ocean, Zhanjiang 524088, China

[3] Key Laboratory of Space Ocean Remote Sensing and Application, MNR, Beijing, 100081, China

[4] Department of Atmospheric and Oceanic Science, University of Maryland, College Park, MD 20742, USA

*Corresponding author.

E-mail address: L. Xie (xiell@gdou.edu.cn)

Abstract

This study aims to analyze statistical behavior of the continental shelf wave motions, including continental shelf waves (CSWs) and arrested topographic wave (ATW), in the northern South China Sea. The baseline consists of tide-gauge data from stations Kanmen, Xiamen, Shanwei, Hongkong, and Zhapo, as well as along-track sea level anomaly (SLA) data derived from multiple satellite altimeters from 1993 to 2020. The subtidal signals propagating along the coast with periods shorter than 40 d and phase speeds of about 10 m s^{-1} are interpreted as CSWs. The cross-shelf structure of along-track SLA indicates that mode 1 of CSWs is the predominant component trapped in the area shallower than about 200 m. The amplitudes of CSWs reach the maximum 0.6 m during July-September, and minimum 0.2 m during April-June. The inter-seasonal and seasonal signals represent ATWs. The amplitudes of ATWs reach 0.10 m during October-December, twice of that during July-September. These observations are well interpreted by the framework of linear wave theory. The cross-shelf structures of CSWs and ATWs derived from along-track SLA illustrate that the methods are suitable

for observing dynamic behavior of the CSWs.

Keywords: Continental shelf wave; Arrested topographic wave; Cross-shelf SLA structure; South China Sea

1 Introduction

Continental shelf wave (CSW) is a type of topographic Rossby wave (TRW) trapped in the continental shelf with amplitudes ranging from several tens' centimeters to more than one meter (Aydın and Beşiktepe, 2022; Clarke and Brink, 1985; Heaps et al., 1988; Morey et al., 2006; Mysak, 1980; Robinson, 1964; Zheng et al., 2015). CSW is a sub-inertial motion with a wavelength much greater than the depth (Li et al., 2015; Schulz et al., 2011). It propagates along the shelf with the coast on its right (left) in the northern (southern) hemisphere (Clarke, 1977). During the impact of typhoon, an excessive flooding in the coastal zone could be induced by a propagating CSW that added to the locally wind-generated surge (Dukhovskoy and Morey, 2011; Han et al., 2012). Therefore, CSW is particularly important for coastal sea-level variations.

CSW is generally generated by large-scale weather systems moving across or along the shelf (Thiebaut and Vennell, 2010). CSW events have been reported by previous investigators lasted from 2 days to 2 weeks (Chen and Su, 1987; Li et al., 2015; Li et al., 2021; Zheng et al., 2015). The phase speed of CSWs depends on the bottom topography, ranging from 5 to 20 m s^{-1} (Li et al., 2015; Li et al., 2016; Shen et al., 2021). CSWs could be taken as barotropic motions in a homogeneous coastal area. While in a stratified ocean, it could be classified into coastal trapped waves. Overall, they are resulting from conserving potential vorticity over the shelf (Chen et al., 2022; Quan et al., 2021; Wang and Mooers, 1976).

The sea level variations in the South China Sea (SCS) are well depicted by these previous studies as the continental shelf occupies about its half area (Ding et al., 2012; Li et al., 2023b; Shen et al., 2021; Zhao et al., 2017; Zhou et al., 2023). However, two issues should be improved. The first is that the primary data are usually obtained from the tide-gauge stations along the coastline. The data have high accuracies, but represent

60 the sea level at the coasts only. Thus, satellite-altimeter-observed the sea level variations

61 are often used to fill the data gaps in between the tide-gauge stations and on the

62 continental shelf. The second issue is that the repeat period of the satellite altimeter is

63 9.9 d, which is challenging to investigate the sea level variations with periods shorter

64 than 10 d. Previous studies used the along-track sea level anomaly (SLA) from satellite

65 altimeters to describe CSW (Chen et al., 2014; Li et al., 2016). However, the satellite

66 altimeter with the sparse tracks (as shown in Fig. 1) could only capture the cross-

67 structure of CSW with one or two snapshots of one CSW.

68

69
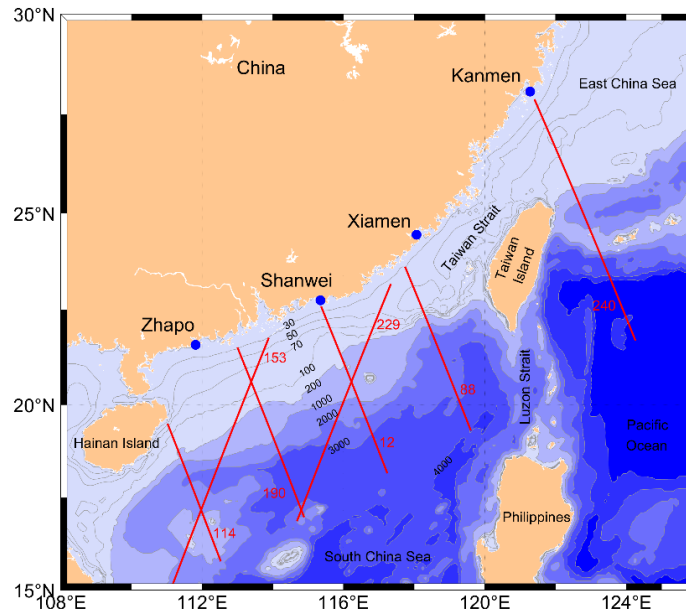
Fig. 1. Study area. Blue dots represent locations of tide-gauge stations Kanmen, Xiamen, Shanwei, and Zhapo. Red lines represent segments of ground tracks 12, 88, 114, 153, 190, 229, and 240 for altimeter satellites over the continental shelf. Tracks 12, 88,114, and 190 are almost perpendicular to the coastline. Isobaths are in m.

74

75 Under the background of global warming, the sea level variation with very low

76 frequency has been investigated by previous investigators. Ho et al. (2000) found

77 seasonal sea level variability in the SCS using data from a satellite altimeter. Kajikawa

78 and Yasunari (2005) investigated the interannual variability of the intra-seasonal

79 variation over the SCS. Fang et al. (2006) analyzed low sea level along the eastern

80 boundary of the SCS. Zhuang et al. (2010) found strong intra-seasonal variability in the

northern SCS. In addition, the sea level variations are influenced by thermodynamic processes, e.g., eddies and thermal change of upper layer of the SCS (Cheng and Qi, 2007; Xie et al., 2018; Zheng et al., 2014).

Meanwhile, the upper layer thermal changes significantly influence the sea level variations (Cheng and Qi, 2007). Using sea surface height (SSH) data from satellite altimeters, Xu et al. (2016) found that sea level variations in the coastal area of the SCS are still strongly influenced by the coastal current system in summer and winter. Seasonal circulation is mainly driven by the monsoon wind stress (Gan et al., 2006). Lin et al. (2021) applied the arrested topographic waves (ATWs) model to the coastal mean dynamic topography along the East China Sea (ECS) and SCS. The mean circulation in a coastal zone of variable depth may be modeled by linear equations (Wu, 2021). The result suggests that the mean dynamic topography is a counterbalance of contributions from the along-shelf wind and bottom friction and well predicted by the ATW model. Therefore, the monsoon winds are a control factor for the sea level variation.

This study aims to investigate the cross-shelf structures of sea level over the continental shelf. As the repeat period of the satellite altimeters, 9.9 d, is comparable with that of CSWs in the northern SCS, the statistical characteristics of the along-track SLA are applied to show the cross-shelf structure of CSWs using a long-term data set from 1993 to 2020. To figure out the cross-shelf structures of ATWs is another goal.

The rest of the paper is organized as follows: Section 2 describes the observed data. Section 3 presents the theory of CSWs and ATWs. Section 4 presents the characteristics of the signals derived from the tide-gauge data and along-track SLA. Section 5 discusses the CSWs detected from tide-gauge data and the cross-shelf structure of sea level over the continental shelf. Section 6 gives summaries.

2 Data

2.1 Along-track sea level anomaly data

Satellite altimeter along-track SLA data are produced and distributed by the Archiving, Validation, and Interpretation of Satellite Oceanographic Data (AVISO),

111   Centre National d'Etudes Spatiales (CNES) of France. The data from 1993 to 2020 are

112   derived from TOPEX/Poseidon, Jason-1, Jason-2, and Jason-3 measurements. The

113   satellite repeat period is 9.9 d, and the temporal resolution of the along-track data is 1

114   Hz. The along-track SLA is calculated by subtracting the twenty-year mean from the

115   SSH measured by the satellite altimeters. The along-track SLA is low pass filtered using

116   a 7-point moving average. The ground tracks in the study area, 12, 88, 114, 153, 229,

117   and 240, are shown in Fig. 1.

118   Satellite altimetry provides a unique sea level dataset for the coastal sea level

119   research. A few recent studies have stressed the importance of small-scale coastal

120   processes on coastal sea-level variance (Cazenave and Moreira, 2022; Vignudelli et al.,

121   2019). The along-track SLA has been successfully validated and applied to the coast

122   zone by Birol et al. (2021). These studies present the availability of along-track SLA in

123   the coastal zones.

124

125   2.2 Sea level anomaly from tide-gauge

126   The tide-gauge data at stations Kanmen, Xiamen, Shanwei, Hongkong and Zhapo

127   (as shown in Fig. 1) are obtained from the Global Sea Level Observing System

128   (GLOSS). The data cover a period from 1993 to 1997, with a temporal resolution of 1

129   h. De-tided sea level anomaly (DSLA) is calculated by removing tidal signals using a

130   Matlab toolbox (Pawlowicz et al., 2002).

131   The monthly sea level means at stations Xiamen, Shanwei, and Zhapo are obtained

132   from the Permanent Service for Mean Sea Level (PSMSL). Monthly mean data cover

133   periods of 1993-2003, 1993-1994, and 1993-2020 for stations Xiamen, Shanwei, and

134   Zhapo, respectively.

135

136   2.3 Sea surface wind stress

137   Monthly sea surface wind stress is derived from the Copernicus Marine

138   Environment Monitoring Service (CMEMS). The dataset covers a period from 1993 to

139   2020 with a spatial resolution of $0.25^\circ \times 0.25^\circ$. Sea surface wind stress data on the

140   satellite altimeter ground tracks are decomposed into the cross-shelf and along-shelf

141 components. The cross-shelf component is positive seaward and parallel to the satellite

142 altimeter ground tracks (12, 88, 114 and 190). The along-shelf component is positive

143 northward and perpendicular to these satellite altimeter ground tracks.

144

145 2.4 Topographic profile

146   The behavior of CSWs is determined by the topography of the continental shelf

147 and slope, which has been well documented. The topographic profiles along the satellite

148 altimeter ground tracks are extracted from a dataset of ETOPO-2. This study uses one-

149 dimensional linear piecewise functions to fit the topographic profiles along the satellite

150 altimeter ground tracks. The width of the continental shelf, depths of shelf break and

151 deep basin along the tracks are listed in Table 1. The continental shelf break is extracted

152 as the location of maximum change in the gradient of the continental slope.

153

154 Table 1. The width of the continental shelf, depths of shelf break and deep basin along
155 the satellite ground tracks.

Track number	l(km)	H_1(m)	H_2(m)
12	200	-300	-3800
88	178	-200	-2500
114	123	-200	-1800
153	259	-110	-1600
190	247	-255	-3500
229	244	-225	-3500
240	273	-250	-5000

156

157 **3 Theory**

158 3.1 Momentum equation for CSWs

159   The linearized shallow-water equations governing a barotropic ocean on a rotating

160 earth are

161
$$\frac{\partial u}{\partial t} - fv = -g\frac{\partial \eta}{\partial x} + \frac{\tau_s^x - \tau_b^x}{\rho H} \tag{1a}$$

162
$$\frac{\partial v}{\partial t} + fu = -g\frac{\partial \eta}{\partial y} + \frac{\tau_s^y - \tau_b^y}{\rho H} \tag{1b}$$

$$\frac{\partial \eta}{\partial t} + \frac{\partial (uH)}{\partial x} + \frac{\partial (vH)}{\partial y} = 0 \tag{1c}$$

where cross-shelf and along-shelf velocities (u, v) are depth-averaged in cross-shelf and along-shelf coordinates (x, y). η is the sea surface height. The Coriolis parameter is f. The bathymetry $H=H(x)$ is assumed to be a function of the cross-shelf variable, x only. τ_s and τ_b the surface and bottom stresses. g, ρ are the gravitational acceleration and the water density.

The scales of the along-shelf length of CSW ($L = 2\pi/k \approx 2 \times 10^3$ km), and cross-shelf length ($l \approx 200$ km) are subject to the long-wave assumption ($l/L \ll 1$). Under the long-wave assumption, a nondimensionalized could be applied to Eqs. (1a-b). Then, $\partial u/\partial t \ll fv$. We neglect the $\partial u/\partial t$ term, and Eqs. (1a-b) become (Li et al., 2016; Schulz et al., 2011):

$$v = \frac{g}{f}\frac{\partial \eta}{\partial x} - \frac{\tau_s^x - \tau_b^x}{f\rho H} \tag{2a}$$

$$u = -\frac{g}{f}\frac{\partial \eta}{\partial y} - \frac{\partial}{\partial t}\left(\frac{g}{f^2}\frac{\partial \eta}{\partial x} - \frac{\tau_s^x - \tau_b^x}{f^2 \rho H}\right) + \frac{\tau_s^y - \tau_b^y}{f\rho H} \tag{2b}$$

Substitute Eqs. (2a-b) into Eq. (1c), we obtain the equation governing SSH of CSWs

$$\frac{\partial}{\partial t}\left(\eta - \frac{gH}{f^2}\frac{\partial^2 \eta}{\partial x^2} - \frac{g}{f^2}\frac{\partial \eta}{\partial x}\frac{dH}{dx}\right) - \frac{g}{f}\frac{\partial \eta}{\partial y}\frac{dH}{dx} + \frac{\partial}{\partial x}\left(\frac{\tau_s^y - \tau_b^y}{f\rho}\right) + \frac{\partial^2}{\partial t \partial x}\left(\frac{\tau_s^x - \tau_b^x}{f^2 \rho}\right) - H\frac{\partial}{\partial y}\left(\frac{\tau_s^x - \tau_b^x}{f\rho H}\right) = 0 \tag{3}$$

Assume that CSWs are forced by along-shelf wind stress, i.e., $\left(\tau_s^x, \tau_s^y\right) = \left(0, \tau_s^y\right)$. The bottom friction is neglected to simplify the calculation in Eq. (3). Therefore, the equation governing the SSH of CSWs becomes

$$\frac{\partial}{\partial t}\left(\eta - \frac{gH}{f^2}\frac{\partial^2 \eta}{\partial x^2} - \frac{g}{f^2}\frac{\partial \eta}{\partial x}\frac{dH}{dx}\right) - \frac{g}{f}\frac{\partial \eta}{\partial y}\frac{dH}{dx} + \frac{\partial}{\partial x}\left(\frac{\tau_s^y}{f\rho}\right) = 0 \tag{4}$$

The change in the SSH of CSWs is balanced by the variation of along-shelf wind stress in cross-shelf direction. Assume a periodic along-shelf wind stress, $\tau_s^y = \tau_0 \exp[i(\alpha y + \omega t)]$ (where α is wavenumber of wind stress, and $\tau_0 = $ constant). Eq. (4) becomes

$$\frac{\partial}{\partial t}\left(\eta - \frac{gH}{f^2}\frac{\partial^2 \eta}{\partial x^2} - \frac{g}{f^2}\frac{\partial \eta}{\partial x}\frac{dH}{dx}\right) - \frac{g}{f}\frac{\partial \eta}{\partial y}\frac{dH}{dx} = 0 \tag{5}$$

which means that the change in SSH is independent of along-shelf wind stress.

190   The assumption of a wave solution

$$\eta = \phi(x)\exp[i(ky + \omega t)] \tag{6}$$

192   yields an equation for $\phi(x)$,

$$H\frac{d^2\phi}{dx^2} + \frac{dH}{dx}\frac{d\phi}{dx} + \left(\frac{fk}{\omega}\frac{dH}{dx} - \frac{f^2}{g}\right)\phi = 0 \tag{7}$$

194

195   3.1.1 Over the shelf

196   For $0 \le x \le l$, $H = H_1 x/l$, the equation for $\phi(x)$ is

$$x\frac{d^2\phi}{dx^2} + \frac{d\phi}{dx} + \left(\frac{fk}{\omega} - \frac{f^2 l}{gH_1}\right)\phi = 0 \tag{8}$$

198   which is subject to the following boundary conditions: $\phi(0) = a$, and $\phi(l) = A$. a and

199   A should be arbitrary. We could take a as the amplitude of fluctuation in sea level from

200   the tidal gauge station.

201   The solution to Eq. (8) is expressed as the sum of the first and second kinds of

202   Bessel functions (Robinson, 1964; Schulz et al., 2011)

$$\phi(x) = aJ_0\left(2\left(\frac{fk}{\omega} - \frac{f^2 l}{gH_1}\right)^{\frac{1}{2}} x^{\frac{1}{2}}\right) + bY_0\left(2\left(\frac{fk}{\omega} - \frac{f^2 l}{gH_1}\right)^{\frac{1}{2}} x^{\frac{1}{2}}\right) \tag{9}$$

204   where a is arbitrary constant. As the solution for $\phi(x)$ is finite, therefore

$$\phi(x) = aJ_0\left(2\left(\frac{fk}{\omega} - \frac{f^2 l}{gH_1}\right)^{\frac{1}{2}} x^{\frac{1}{2}}\right) \tag{10}$$

206

207   3.1.2 In the deep basin

208   For $l < x$, $H = H_2$, the equation for $\phi(x)$ is

$$\frac{d^2\phi}{dx^2} - \frac{f^2}{gH_2}\phi = 0 \tag{11}$$

210   which is subject to the following boundary conditions: $\phi(x \to l) = A$, and $\phi(\infty) = 0$.

211   The solution is

$$\phi(x) = A\exp\left(-\frac{fl}{\sqrt{gH_2}}\left(\frac{x}{l} - 1\right)\right) + B\exp\left(\frac{fl}{\sqrt{gH_2}}\left(\frac{x}{l} - 1\right)\right) \tag{12}$$

213   As the solution for $\phi(x)$ is also finite in the deep basin, i.e.,

$$\phi(x) = A\exp\left(-\frac{fl}{\sqrt{gH_2}}\left(\frac{x}{l} - 1\right)\right) \tag{13}$$

215   where A is arbitrary constant.

216

217   ### 3.1.3 Dispersion relation

218   As the fluid is continuous at the edge of continental shelf, therefore

219
$$H_1 \cdot u|_{x \to l_-} = H_2 \cdot u|_{x \to l_+} \tag{14a}$$

220
$$aJ_0\left(2\left(\frac{fkl}{\omega} - \frac{f^2l^2}{gH_1}\right)^{\frac{1}{2}}\right) = A \tag{14b}$$

221   From Eq. (14a), we have

222
$$H_1 \cdot a\left(kJ_0 + \frac{\omega}{f}\left(\frac{fk}{\omega l} - \frac{f^2}{gH_1}\right)^{\frac{1}{2}} J_0'\right) = H_2 \cdot A\left(k - \frac{\omega}{\sqrt{gH_2}}\right) \tag{15}$$

223   where J_0' is the derivation of the zero-order of the first kind Bessel function,

224
$$J_0'(x) = -\frac{x}{2}\left(J_0(x) + J_2(x)\right) \tag{16}$$

225   where J_2 is the second order of J_0.

226   Substituting Eq. (16) into Eq. (15) yields a dispersion relation for CSWs

227
$$\left(\frac{cfl}{gH_2} - 1 + \frac{c}{(gH_2)^{\frac{1}{2}}}\right)J_0 - \left(\frac{H_1}{H_2} - \frac{cfl}{gH_2}\right)J_2 = 0 \tag{17}$$

228   where $c\ (=\frac{\omega}{k})$ is phase speed of CSWs. We solve Eq. (17) using the zero-finding

229   function in MATLAB. The solution of phase speed for CSWs is shown as Fig. 2. The

230   zero-crossing points for each curve present the phase speed of CSWs. The first zero-

231   crossing point on the right hand of each curve points out the phase speed of mode-1

232   CSW, e.g., $c = 7.6$ m s^{-1} for track 190.

233
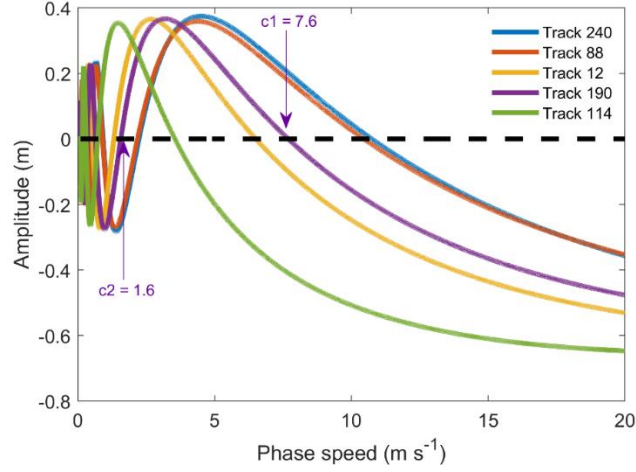
234
235 **Fig. 2.** Solution of phase speed for CSWs from Eq. (17). The zero-crossing values
236 represent the phase speed of CSWs for different modes. Colorful curves are amplitude
237 of zero-order of the first kind Bessel function in different modes for the idealized depth
238 profile of tracks 12, 88, 114, 190, and 240, respectively. Arrows point out the phase
239 speed of mode-1 (7.6 m s^{-1}) and mode-2 (1.6 m s^{-1}) CSWs along track 190.

240

241 3.1.4 Cross-shelf structure

242   With Eqs. (10), (13) and (14b), the wave solution of SSH, i.e., Eq. (3), is

243
$$
\eta = \begin{cases}
\sum_{i=1}^{\infty} a_i \cdot J_0 \left(2 \left(\frac{fk_i}{\omega_i} - \frac{f^2 l}{gH_1} \right)^{\frac{1}{2}} x^{\frac{1}{2}} \right) \exp[i(k_i y + \omega_i t)] & x \le l \\[4mm]
\sum_{i=1}^{\infty} a_i \cdot J_0 \left(2 \left(\frac{fk_i l}{\omega_i} - \frac{f^2 l^2}{gH_1} \right)^{\frac{1}{2}} \right) \exp \left(-\frac{fl}{\sqrt{gH_2}} \left(\frac{x}{l} - 1 \right) \right) \exp[i(k_i y + \omega_i t)] & x > l
\end{cases}
$$

244   (18)

245 where $\exp[i(ky + \omega t)]$ is the waveform propagating along the shelf. $a_i \cdot J_0$ is the

246 cross-shelf structure of the waveform for mode i over the shelf.

247   In the cross-shelf direction, the SSH becomes

248
$$
\eta = \begin{cases}
\sum_{i=1}^{\infty} \eta_{0i}(t) \cdot J_0 \left(2 \left(\frac{fk_i}{\omega_i} - \frac{f^2 l}{gH_1} \right)^{\frac{1}{2}} x^{\frac{1}{2}} \right) & x \le l \\[4mm]
\sum_{i=1}^{\infty} \eta_{0i}(t) \cdot J_0 \left(2 \left(\frac{fk_i l}{\omega_i} - \frac{f^2 l^2}{gH_1} \right)^{\frac{1}{2}} \right) \exp \left(-\frac{fl}{\sqrt{gH_2}} \left(\frac{x}{l} - 1 \right) \right) & x > l
\end{cases}
\qquad (19)
$$

249 where $\eta_{0i}(t) (= a_i \exp[i(k_i y + \omega_i t)])$ is time series of SSH at the coastline for mode

250 i.

251   Fig. 3 shows the SSH structure over the continental shelf. The SSH mode 1 looks

252 like a bell mouth. For Modes 2 and 3, nodes and antinodes appear on the shelf. Node

253 for Mode 2 appears at 50 km off the coast over the shelf. Nodes for Mode 3 appear at

254 30 and 90 km off the coast.

255
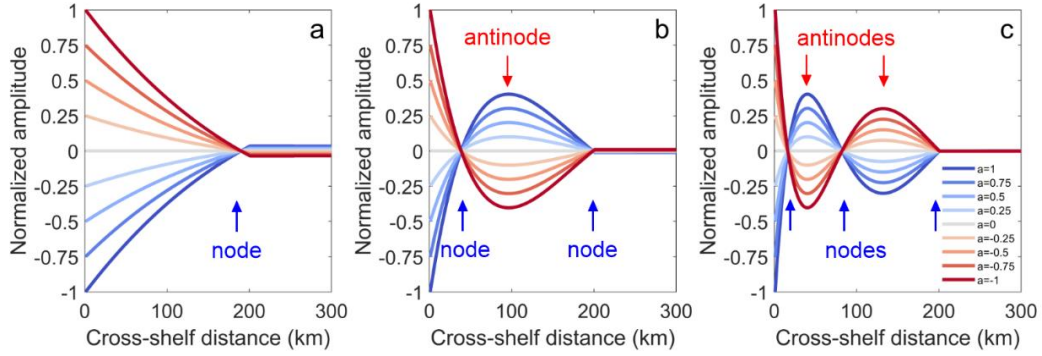
256
257 **Fig. 3.** (a-c) Cross-shelf structure of normalized amplitudes of the first three CSW
258 modes for idealized depth profile of track 12. Gradient color curves represent amplitude
259 structure over time for CSWs in the cross-shelf direction.

260

261 3.2 Steady situation

262   The governing equations in the steady situation for Eqs. (1a-c) are

263
$$-fv = -g\frac{\partial \eta}{\partial x} \tag{20a}$$

264
$$fu = -g\frac{\partial \eta}{\partial y} + \frac{\tau_s^y - \tau_b^y}{\rho H} \tag{20b}$$

265
$$\frac{\partial(uH)}{\partial x} + \frac{\partial(vH)}{\partial y} = 0 \tag{20c}$$

266 A linear drag is used for the bottom friction, i.e., $\vec{\tau_b} = \rho\lambda\vec{u}$ (Hsueh and Pang, 1989; Lin

267 and Yang, 2011).The solution for SSH based on Eqs. (20a-c) gives (Csanady, 1978)

268
$$\eta = B\tau_0 e^{-\frac{x}{L}}\sin\left(\alpha y + \frac{x}{L} - \frac{\pi}{4}\right) \tag{21}$$

269 where $L = \sqrt{2\lambda l/\alpha f H_1}$ is the scale width of trapped sea level in the cross-shelf

270 direction, B is an arbitrary constant. A drag coefficient, $\lambda = O(5 \times 10^{-4})$ m s^{-1}, is used

271 for the linear bottom friction (Chapman, 1987; Lin and Yang, 2011). The typical

272 magnitude for winter wind stress over the northern continental shelf of the SCS is

273 $O(0.1)$ N m^{-2} (Lin and Yang, 2011; Lin et al., 2011). $f = 5 \times 10^{-5}$ s[-1], and $\alpha =$

274 $2\pi/4000$ km evaluated by Lin et al. (2021).

275   The normalized SSH in the cross-shelf direction of ATW for tracks 12, 88, 114,

276 and 190 are shown in Fig. 4. One can see that the trapped sea level in the cross-shelf

277 direction decays quickly from 1 at the coastline to ~0.2 at the edge of the continental

278 shelf (~200 km), and 0.1 at a distance of 300 km. The ATW amplitude decays offshore,

279 and $L = $ ~100 km in the study area, which is much less than the local Rossby radius of

280 deformation (~600 km). Under different wind stresses, the amplitude of ATW evolves

281 similarly to that in Fig. 3a. As Track 240 is not perpendicular to the coastline, it is

282 beyond the scope.

283
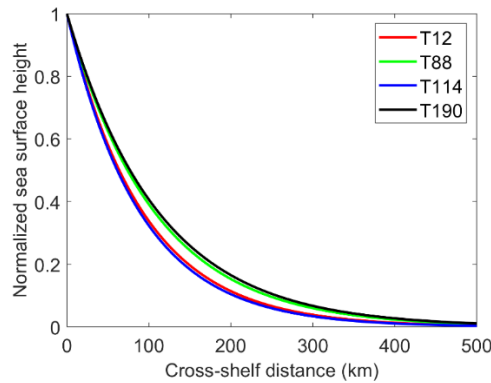
284

285 **Fig. 4.** Normalized SSH in cross-shelf direction for tracks 12, 88, 114, and 190.

286

287 **4 Signals in sea level anomaly**

288 4.1 Tide-gauge data

289 Fig. 5 shows the wavelet transform (WT) of SLA at station Xiamen from 1993 to

290 1997. One can see abundant signals with periods from several days to one year in Figs.

291 5a-b. A dozen signals with periods from several days to about one month could be seen

292 from the WT of SLA every year. The duration of these signals, with a period of several

293 days, is about ten days (e.g., in Fig. 5d). Moreover, the signals with a period of about

294 one month sustain for about three months (Figs. 5c-d). Even if significance level against

295 red noise is larger than 5%, the power is universal and continuous in the period bands

296 of 10-60 d. The main reason is that these signals are not so significant compared with

297 the signals with large amplitude. The wavelet analysis also exhibits a significant inter-

298 seasonal and seasonal variation of SLA. The characteristics of the signals at stations

299 Kanmen, Shanwei, and Zhapo are almost the same (not shown here). Therefore, the

300 variation of SLA along the northern SCS coast is universal.

301
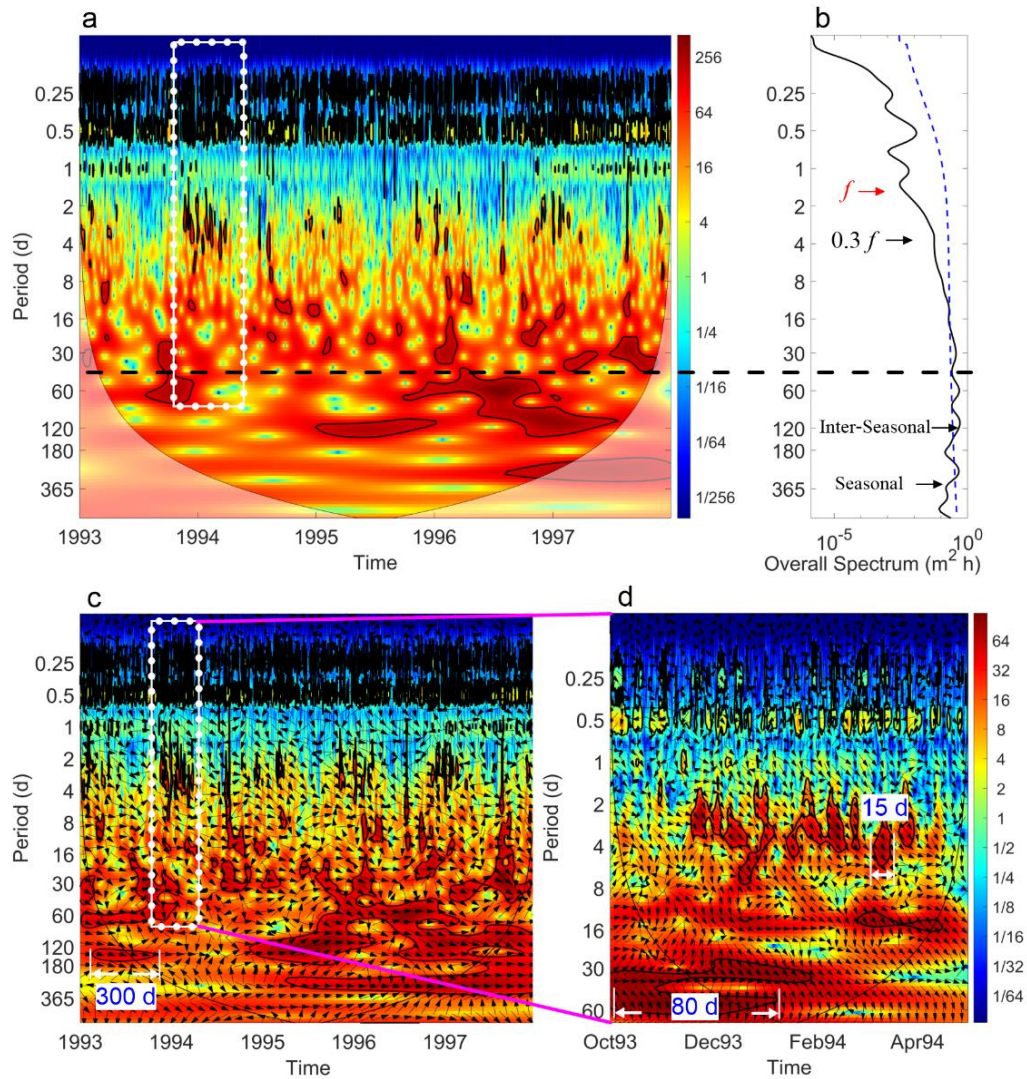
Fig. 5. Temporal variability of SLA at the coastline. (a) WT of SLA at station Xiamen. (b) Overall spectrum of SLA at station Xiamen. (c) XWT of SLA between stations Kanmen and Xiamen. (d) XWT of SLA between stations Kanmen and Xiamen from October 1993 to April 1994. White line and arrows are auxiliary lines pointed out duration. The thick line is a 5% significance level against red noise, and the cone of influence (COI) is shown as the thin line. Color codes of power spectra normalized by variance are in arbitrary units. White dotted rectangles in (a) and (c) show the temporal domain of (d). The Blue dashed curve in (b) is a 5% significance level. Arrows in (b) point out the characteristic frequencies of inertial oscillation and CSWs. The black dashed lines in (a) and (b) represent signal period boundary (40 d). The arrows in (c) and (d) show the relative phase relationship between SLA at Kanmen and Xiamen with in-phase (anti-phase, leading, and lagging) pointing right (left, down, and up). In (d), arrows point down-right (about $\pi/3$), indicating SLA in Kanmen is leading that in Xiamen.

Figs. 5c-d show the cross wavelet transform (XWT) of SLA between stations

319   Kanmen and Xiamen. One can see that the period band and the occurrence time of the

320   significant cross wavelet power are consistent with that in Fig. 5a. The signals with

321   periods shorter and longer than 40 d show remarkably different characteristics. In the

322   period band shorter than 40 d, one can see the arrows generally point down-right. The

323   quasi-uniform phase lag indicates the fixed time delay of the signal between two tidal

324   gauge stations. However, the direction of arrows is in disorder for the period band

325   longer than 40 d, which indicates there is no evidence for propagating.

326   In the period band shorter than 40 d, the signals at station Xiamen lag that at station

327   Kanmen about 15 h (time lag=phase difference/$2\pi\times$period of signal). The propagation

328   phase speed of the sea level signal could be calculated by the lag time of sea level

329   propagation between stations Kanmen and Xiamen. The result is about 9 m s^{-1}, which

330   is very close to that reported by a number of recent studies (Ding et al., 2012; Li et al.,

331   2015; Li et al., 2016; Zhao et al., 2017).

332   In the period band longer than 40 d, the phase of signals between Kanmen and

333   Xiamen is a little complicated. The signal phase with the period of 360 d from 1995 to

334   1997 is almost 0. However, the seasonal signals at station Xiamen lag (lead) that at

335   station Kanmen in winter (summer) about $\pi/4$-$\pi/2$, implying that the signal propagates

336   very slowly along the coast. Csanady (1978) concluded that these signals are a kind of

337   ATWs.

338

339   4.2 Along-track SLA

340   Fig. 6 shows the latitudinal distribution of the along-track SLA over the northern

341   continental shelf of the SCS from 1993 to 2020. One can see the clear annual signals

342   near the coast in Figs. 6a-g. Signals with periods shorter than one year could also be

343   seen. As shown in Figs. 6h-n, a clear seasonal cycle is discernable from the

344   climatological monthly mean of the along-track SLA. One can see that lower (higher)

345   sea levels over the shelf exist from March to August (September to February). The

346   trough (~-0.2 m) and peak (~0.24 m) of sea level near the coast occur in July and

347   October, respectively. While in track 240, climatological monthly mean of the along-

348   track SLA on the shelf is smaller than that in track 88 especially in July. The 28-year

349 mean value of the along-track SLA is about 0.04 m, as shown in Figs. 6o-u.

350

351
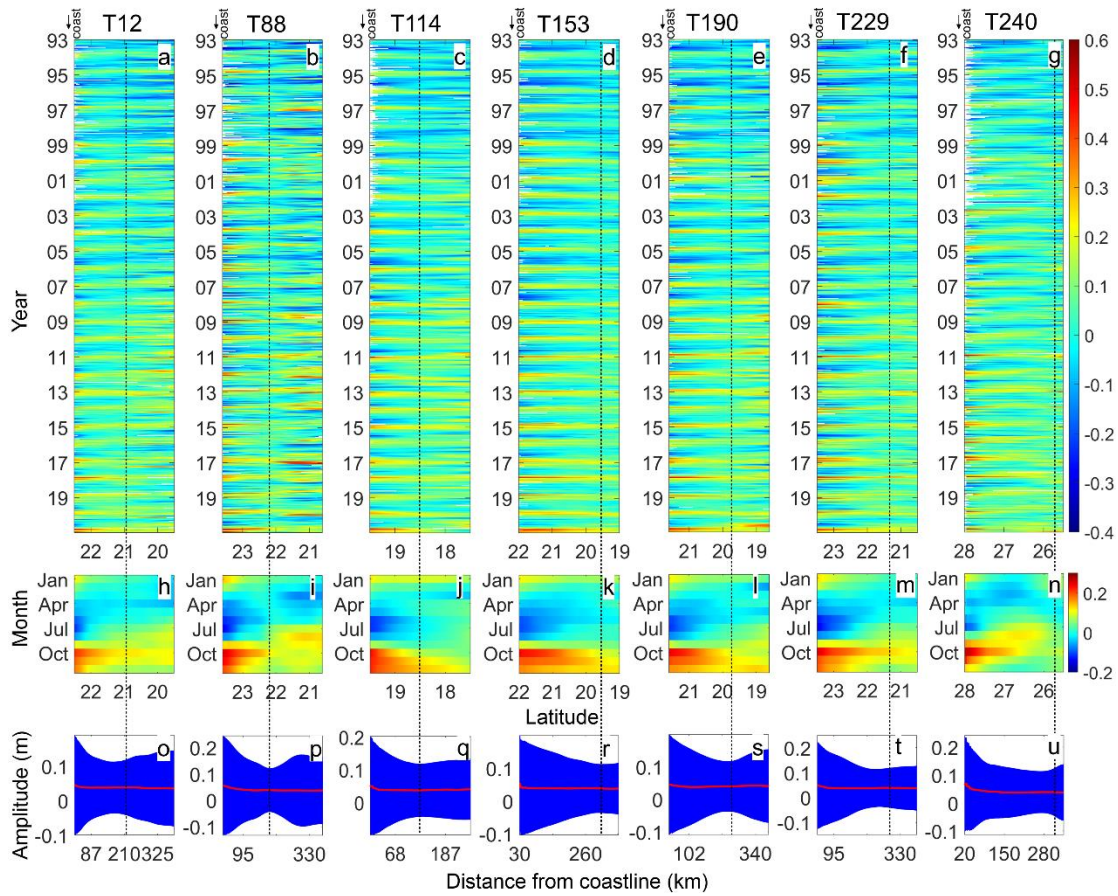
Fig. 6. (a-g) Latitudinal distribution of the along-track SLA over the northern continental shelf of the SCS from 1993 to 2020 for tracks 12, 88, 114, 153, 190, 229, and 240, respectively. (h-n) Climatological monthly mean of the along-track SLAs for Tracks 12, 88, 114, 153, 190, 229, and 240. (o-u) Mean (red curves) and standard deviation (blue shadow) of the along-track SLA from 1993 to 2020 for tracks 12, 88, 114, 153, 190, 229, and 240. Track numbers are shown on the tops of panels. Vertical dashed lines represent shelf break positions along the tracks, i.e., H_1, listed in Table 1. The coastline position is marked by an arrow on top left of each panel.

360

361   Moreover, the standard deviations (STD) of the along-track SLA from 1993 to

362 2020 (blue shadow in Figs. 6o-u) show a bell-mouth-like structure over the shelf. The

363 amplitudes of the along-track SLA reach the maxima near the coast. The minimum

364 variance exists near the shelf edge. The cross-shelf structure of SLA indicates that sea-

365 level signals depend on the shelf depth.

366

367 **5 Discussion**

368 5.1 Propagation of CSWs

369   Fig. 7 compares the data derived from the XWT of SLA with the dispersion

370 relation of CSW. We overlay the dispersion relation curves of CSWs with the results

371 (phase speed, c and period, T, $\lambda = c \cdot T$) from tide-gauge data analysis in Section 4.1.

372 One can see that the data points derived from station pairs are distributed near the

373 dispersion relation of CSWs, implying the signals with the periods shorter than 40 d are

374 the CSWs propagating along the shelf.

375
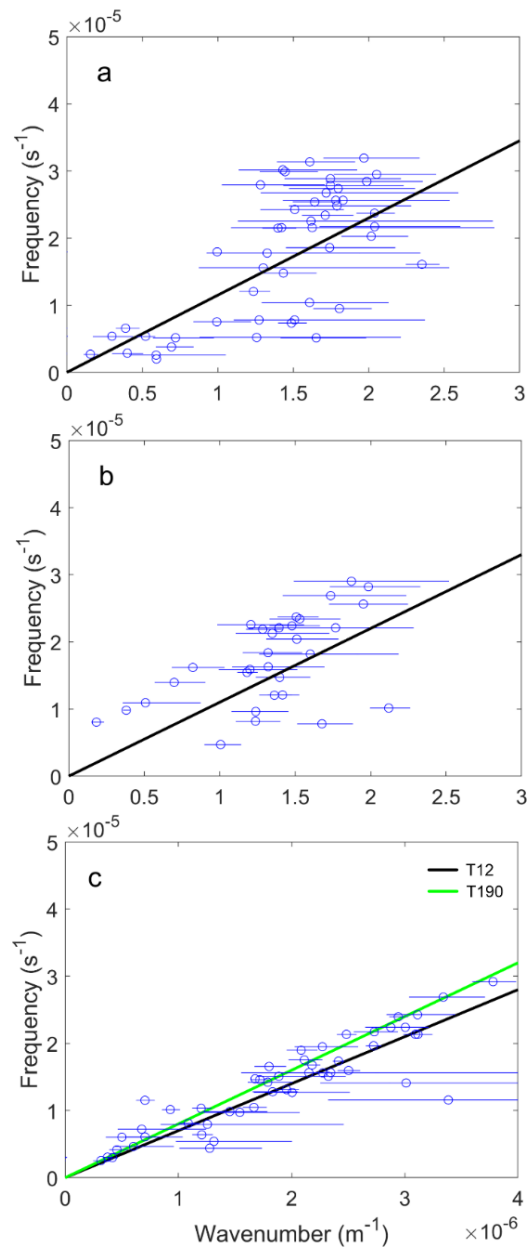
376
377 **Fig. 7.** Dispersion relation of the lowest mode of CSWs between (a) Kanmen and
378 Xiamen, (b), Xiamen and Shanwei, as well as (c) Shanwei and Zhapo. The data points

379 are calculated from the XWT of SLA. The curves are the theoretical dispersion relation
380 for the mean depth profiles listed in Table 1. Black and green curves in (c) represent the
381 dispersion relation (from Fig. 2) for the topographic profiles along tracks 12 and 190

382

383   Figs. 7a-b deal with the signals between Kanmen and Shanwei. We use the

384 bathymetric profile near Track 240 and 88 of the altimeter satellite to calculate the

385 dispersion relation curve, respectively. However, since the topography between

386 Kanmen and Shanwei changes dramatically, the data points lie dispersedly around the

387 curve. The wavenumbers of CSWs range from 0.1 to 2.4 $\times 10^{-5}$ m^{-1} between stations

388 Kanmen and Shanwei. The CSWs propagate along the coast with a phase speed of 10

389 m s^{-1}.

390   Fig. 7c shows the signals between Shanwei and Zhapo. The data points and the

391 theoretical curves agree quite well. Compared with the topography between Kanmen

392 and Shanwei, the topography changes slightly between stations Shanwei and Zhapo.

393 Thus, we conclude that the signals in tide-gauge data with the periods shorter than 40

394 d are the CSWs propagating along the shelf. The phase speed of CSWs is about 8 m s^{-1}

395 ^{1} in the study area, which is close to that of previous studies (Li et al., 2015; Li et al.,

396 2016; Shen et al., 2021).

397   Previous studies present that the periods of CSWs range from two days to two

398 weeks in the SCS (Chen and Su, 1987; Li, 1993). The period of CSWs upstream, i.e.,

399 in the ECS, is often detected as several days (Ding et al., 2012; Ding et al., 2018; Hsueh

400 and Pang, 1989; Huang et al., 2015; Yin et al., 2014). Hsueh and Romea (1983) found

401 the sea level fluctuations with a period of more than 13 d along the West Korean coast.

402 Worldwide, these low-frequency CSWs are common along the coast of Chile and the

403 east coast of the Indian Ocean (Castro and Lee, 1995; Hormazabal et al., 2001; Marshall

404 and Hendon, 2013; Vialard et al., 2009), where the width of the continental shelf is

405 narrow. In this study, we define the CSW with a maximum period of about 30-40 d. The

406 main reason for the difference is the data length we used. The long-time series of DSLA

407 helps analyze the abnormal low-frequency CSWs in the SCS.

408   In addition, we should take care that CSWs in Fig. 7 are mixed with wind-forced

409 CSWs. It is difficult to separate the effect of wind-force and free propagating CSWs

410 clearly. Hsueh and Romea (1983) found that there is a clear coupling between surface

411 winds and coastal sea level in the northeast China Sea. Li et al. (2016) found that the

412 propagation time of the wind signals are much shorter than that of CSWs in the north

413 SCS. Even though one can see isolated cases which are away from the dispersion

414 relationship of CSW in Fig. 7, most of the data points are near the theoretical dispersion

415 relation. Moreover, the stratification in the continental shelf is important for the

416 characteristics of CSW. The sea level variation in this study should show coastal trapped

417 waves influenced by stratification.

418

419 5.2 Trapped cross-shelf structure

420 5.2.1 CSWs

421   As the sampling period of the altimeter satellites is about 10 d, the signals with

422 periods shorter than 20 d could not be distinguished from the along-track SLA based

423 on the Nyquist sampling theorem. Fortunately, the cross-shelf structure of CSWs could

424 be sampled as fragments by repeat satellite observations.

425   In this case, the CSWs with a period less than 40 d were abundant from 1993 to

426 2020 on the northern continental shelf of the SCS, especially in winter (Fig. 5). Even if

427 the significance level is larger than 5%, the power is universal and continuous in this

428 period band. Therefore, it could be considered that a large number of repeat

429 observations by altimeter satellites were executed during CSW events.

430   Fig. 8 shows a boxplot of the along-track SLA over the continental shelf for tracks

431 12, 88, 114, and 190. The maxima, minima, and outliers derived from Fig. 8 are listed

432 in Table 2. The whisker dashed black line outside of the box extends to the most extreme

433 data points. One can see that the trapped characteristics as the maximum amplitude

434 (75th percentile), interquartile range (IQR), and outliers (red cross sign) occur at the

435 coastal side. In contrast, the minima occur at the edge of the continental shelf (150, 165,

436 105, and 165 km offshore for tracks 12, 88, 114, and 190). The amplitude of the along-

437 track SLA for maxima and IQR decreases gradually from the coastline (0.2-0.4 m) to

438 the edge of the continental shelf (~0.1 m). The largest outlier is 0.65 m over the shelf

439 30 km offshore.

440
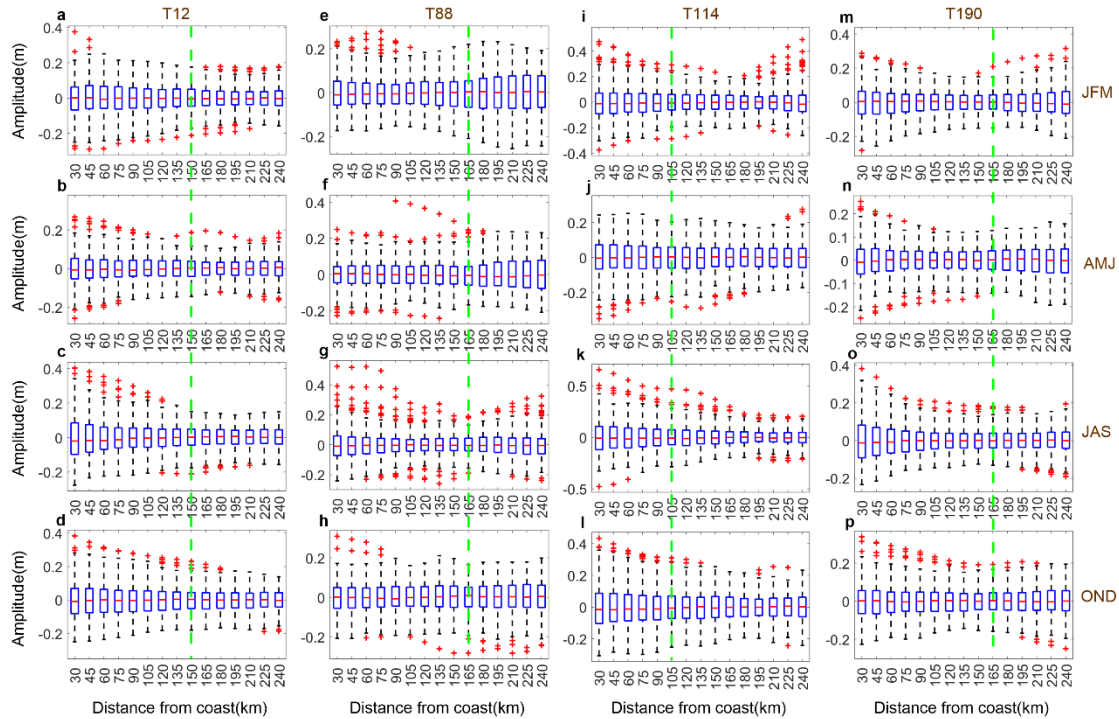
441

442 **Fig. 8.** Boxplot of the along-track SLA on the shelf for tracks 12, 88, 114, and 190 from
443 1993 to 2020 (in the column). Seasonal means of SLA are plotted in the rows. Green
444 dashed lines present the minimum STD of the along-track SLA. The climatological
445 seasonal mean is removed. The along-track SLA is averaged for each 15 km offshore.
446 In each box, the central red line indicates the median, and the bottom and top edges of
447 the blue box indicate the 25th (Q1) and 75th (Q3) percentiles, respectively. The upper
448 (Q3+1.5IQR) and lower (Q1-1.5IQR) whiskers extend to the most extreme data points
449 not considered outliers. The outliers are the most extreme data points (larger than upper
450 whisker or smaller than lower whisker), plotted individually using the red cross marker.
451 IQR= Q3-Q1.
452
453 Table 2. Parameters extracted from along-track SLA in Fig. 8.

Position *	Track (Distance)**	T12 (150 km)				T88 (165 km)				T114 (105 km)				T190 (165 km)			
	Month	JFM	AMJ	JAS	OND	JFM	AMJ	JAS	OND	JFM	AMJ	JAS	OND	JFM	AMJ	JAS	OND
Coast	Outlier(m)	0.28	0.25	0.38	0.34	0.47	-0.35	0.65	0.43	0.23	0.24	0.52	0.31	0.38	0.27	0.41	0.38
	Max (m)	0.26	0.19	0.32	0.24	0.29	0.24	0.42	0.36	0.21	0.17	0.25	0.18	0.21	0.19	0.34	0.28
	Min (m)	-0.23	-0.22	-0.24	-0.23	-0.3	-0.24	-0.33	-0.31	-0.17	-0.18	-0.24	-0.2	-0.25	-0.21	-0.28	-0.25

Edge	Outlier(m)	0.17	-0.15	0.19	0.19	0.23	-	0.29	-	0.21	0.39	0.28	0.16	-0.2	0.2	-0.2	0.21
	Max (m)	0.15	0.12	0.13	0.16	0.16	0.2	0.2	0.22	0.17	0.18	0.15	-0.18	0.16	0.12	0.14	0.17
	Min (m)	-0.15	-0.14	-0.13	-0.15	-0.19	-0.2	-0.2	-0.21	-0.16	-0.14	-0.15	-0.2	-0.17	-0.13	-0.16	-0.17

454 *Coast is the position with the highest STD for each track, about 15 km offshore. Edge

455 is the position with the minimum STD of the along-track SLA as shown in Fig. 8.

456 ** Distance between coastline and edge.

457

458   The largest SLAs over the shelf occur from July to September. For example, the

459 75th percentile of SLAs near the coastline is about 0.25 m for track 144, and 0.42 m for

460 track 88. The largest outlier of 0.65 m also occurs from July to September for track 88.

461 The smallest SLA occurs from April to June when the wind is weak during the monsoon

462 transition period (Wang et al., 2009). The extreme data from July to September show

463 the occurrences of storm surges over the shelf (Chen et al., 2014).

464   Overall, the maximum amplitude, IQR, and extreme data of the along-track data

465 over the shelf show the trapped wave characteristics, which shows that SLA decreases

466 gradually from the coastline to the edge of the continental shelf. The trapped

467 characteristics from the along-track SLA are similar to the cross-shelf structure of

468 normalized amplitudes of the mode 1 CSWs, as shown in Fig. 3a. The along-track SLA

469 should contain higher modes. The along-track SLA along tracks 153 and 229 show

470 similar characteristics (not shown). That along track 240 (as shown in Fig. 6n) presents

471 a differentiated pattern in the coast side and shelf edge during May-July. The main

472 reason should be the existence of cold eddy in the north of Taiwan Island.

473   To further reveal the variations in the along-track SLA in track 12 on the shelf, the

474 empirical orthogonal function (EOF) analysis results are shown in Fig. 9 (EOF analysis

475 for data along other tracks is similar, not shown here). The first four EOF modes of the

476 along-track SLA explain 96.8% of the total variance. Mode 1 explains the seasonal

477 variance of SSH (red curve in Figs. 6o-u). The seasonal cycle could be characterized

478 clearly from Fig. 9b, with peaks in October and troughs in May. Mode 2 and Mode 3

479 are similar to the cross-shelf structure as shown in Fig. 3a, which explains 25.1% of the

480 total variance. Mode 3 is influenced by the background of SSH in the open sea side.

481   The amplitude is 0.3-0.4 m, which is comparable to the outlier data as shown in Table

482   2. Mode 4 is similar to the cross-shelf structure of mode-2 CSW as shown in Fig. 3b,

483   which only explains 2.8% of the total variance. The EOF analysis indicates that CSW

484   could explain <30% of the total variance of SSH in the study area, which is comparable

485   to the IQR in boxplot of the along-track SLA (Fig. 8).

486
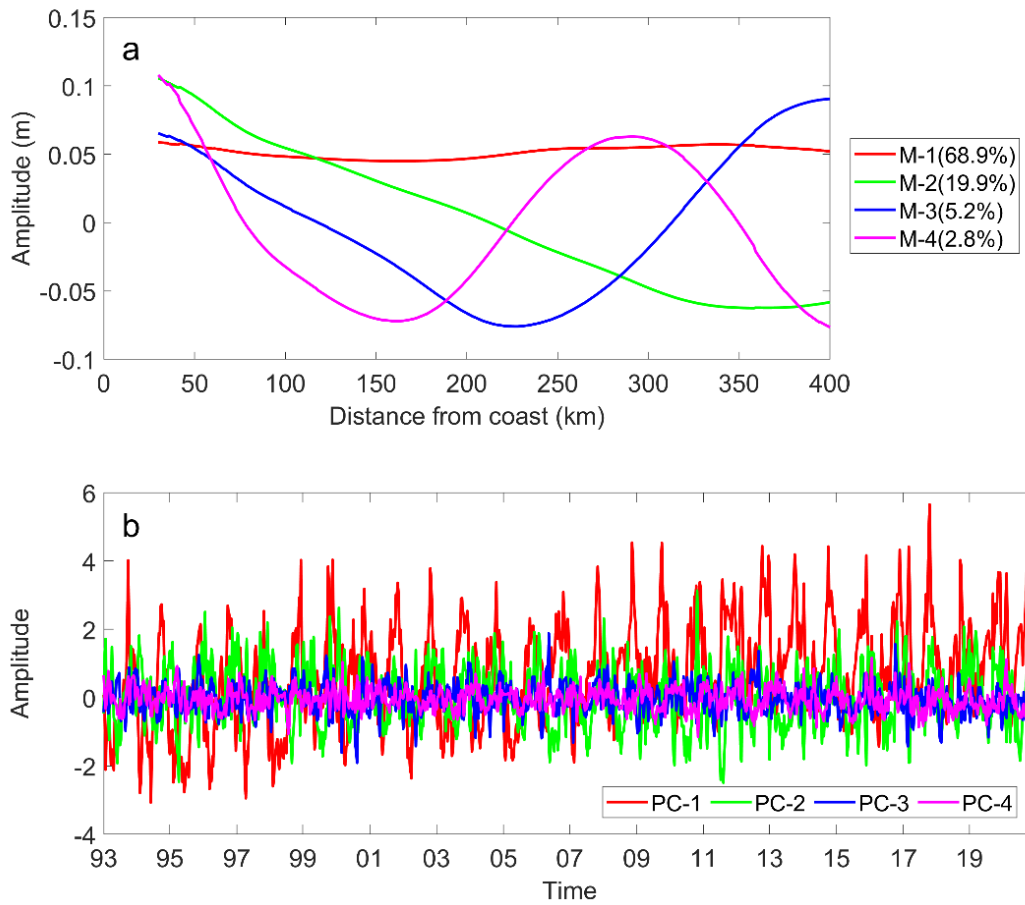
487

488   **Fig. 9.** The first four EOFs for the along-track SLA on the shelf along track 12. Cross-

489   shelf amplitude (a) and time series (b) of EOFs. The variance explained by each mode

490   is labeled in (a).

491

492   5.2.2 ATWs

493   As shown in Fig. 6, the inter-seasonal and seasonal signals could be distinguished

494   from along-track SLA. Fig. 10 shows the seasonal mean of the along-track SLA and

495   along-shelf sea surface wind. One can see that the time series of the seasonal mean of

496   the along-track SLA show the seasonal variation with the amplitude of 0.1-0.2 m at 15

497   km offshore. The time series of the seasonal mean of DSLA show similar characteristics

498   with the along-track SLA. The correlation relationship between the seasonal mean of

499   the along-track SLA and along-shelf sea surface winds reaches >0.77. The monthly

500   mean of SLA during April-September is negative, while positive in the other months. It

501   is attributed to that the local wind stress substantially influences the coastal sea level

502   (Lin et al., 2022).

503
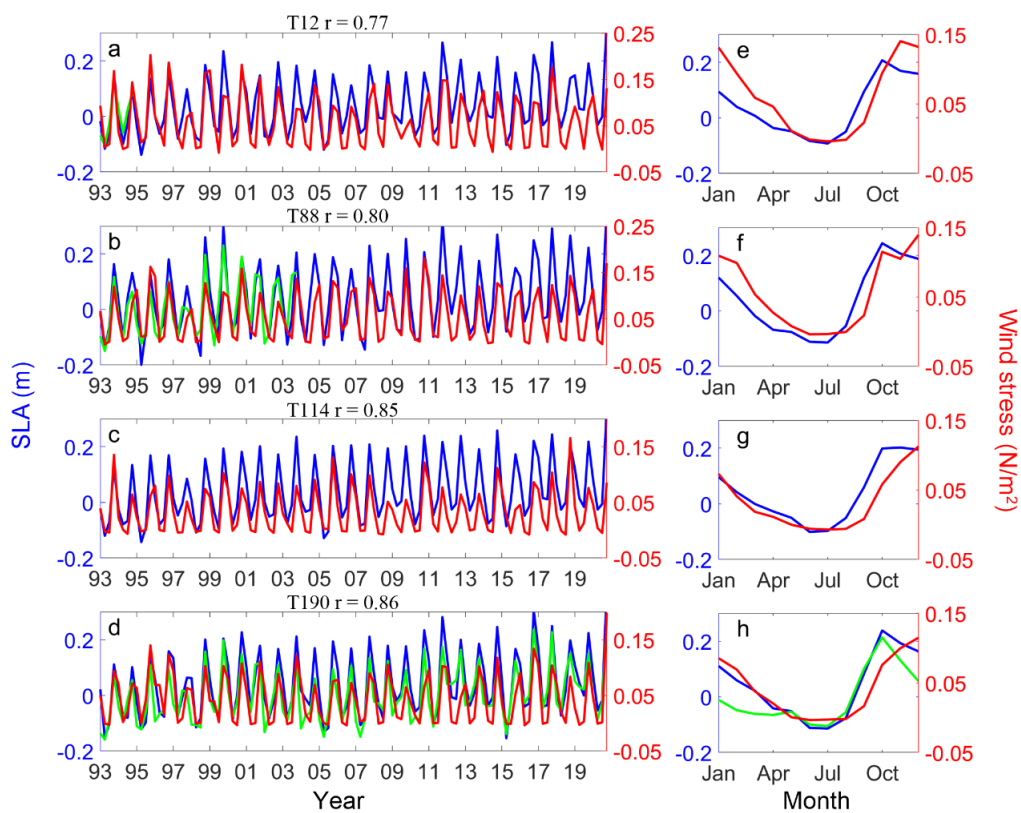
505 **Fig. 10.** Time series of the seasonal mean of the along-track SLA and along-shelf sea
506 surface wind stress for tracks (a)12, (b) 88, (c) 114, (d)190, and (e-h) climatological
507 monthly mean of the along-track SLA and along-shelf sea surface wind stress. Red
508 curves represent the along-track SLA at 15 km offshore. Green curves represent the
509 seasonal mean of sea level data at tide-gauge stations (a) Xiamen, (b) Shanwei, and (d)
510 Zhapo. Green curve in (h) is climatological monthly mean of sea level data at tide-
511 gauge station Zhapo.

512

513   In addition, one can also see a characteristic of out-of-sync between the seasonal

514   mean of the along-track SLA and wind. The maximum mean sea surface wind stress

515   occurs in November and December. While, that of monthly along-track SLA occurs in

516 October. Ding et al. (2020) investigated the seasonality of coastal circulation in the

517 north SCS using a numerical model. The result indicates that the maximum of water

518 transport is 1.93 Sv occurred in autumn. Li et al. (2023a) found the along-shelf current

519 is strongest in October at approximately $0.17\,\mathrm{m\,s^{-1}}$. The along-shelf current involves

520 ATW, which is the reason why there is a difference between monthly climatological

521 mean of the along-track SLA and sea surface wind stress as shown in Figs. 10e-h.

522   Fig. 11 shows the cross structure of the seasonal mean of the along-track SLA.

523 One can see that the SLA on the coastline side is lower than on the ocean side from

524 April to September. In the other seasons, the slope of the along-track SLA is the

525 opposite. The along-track SLA presents similar characteristics as shown in Fig. 10, i.e.,

526 the variation of SLA is controlled by the sea surface winds over the shelf.

527

528
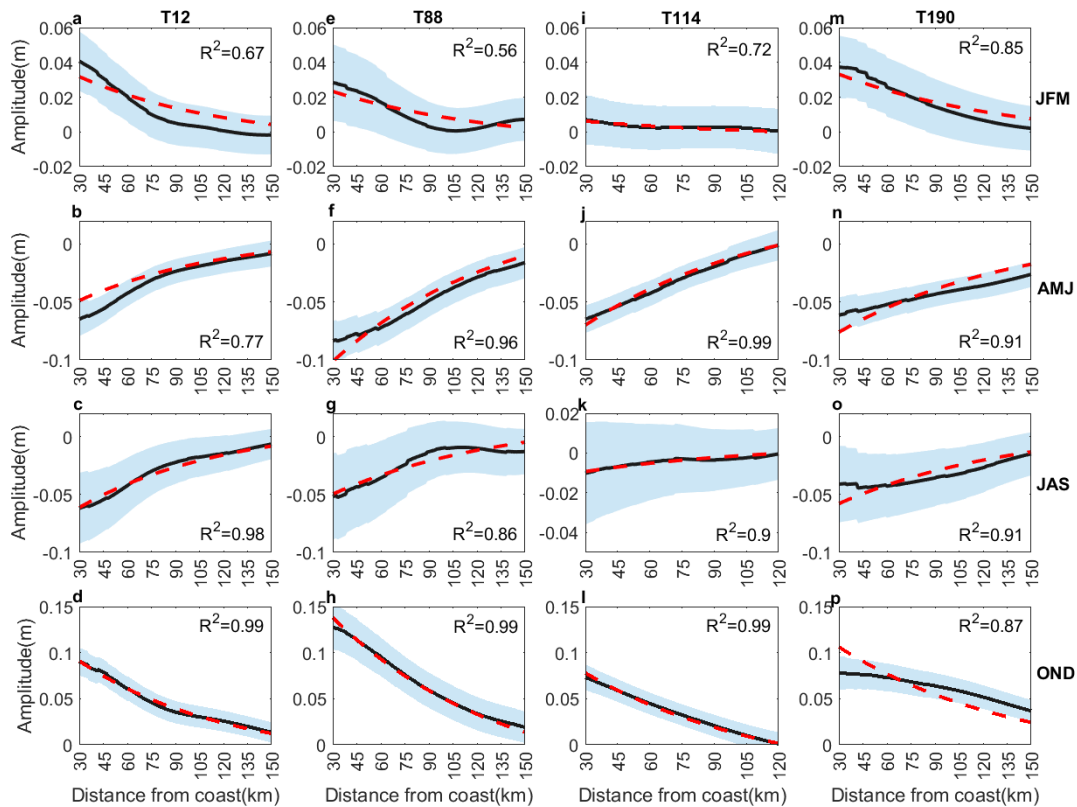
Fig. 11. Fitting climatologic seasonal mean of the along-track SLA (black curves) using
cross-shelf ATWs (red dashed curves) for tracks (a-d) 12, (e-h) 88, (i-l) 114, and (m-p)
190. Dashed shadow is the STD of the seasonal mean of the along-track SLA.

532

533   Meanwhile, from Fig.11 one can see the cross-shelf structure of the along-track

SLA. The fitting curves show that theoretical ATWs (Fig. 4) explain the cross-shore structure of the along-track SLA very well. The amplitudes of ATWs in track 12 are 0.04 m, -0.06 m, -0.05 m, and 0.10 m in January-March, April-June, July-September, and October-December. That along track 88 is relatively larger, e.g., 0.13 m in October-December. While, the minimum amplitude occurs in track 114. Differently from Fig. 8, the amplitudes of ATWs during October-December are larger than that during July-September. It should be attributed that the monsoon winds in winter are stronger than that in summer.

Lin et al. (2021) investigated the tilt of mean dynamic topography along the coast of the Chinese mainland. Wu (2021) used a nondimensional parameter ($Pe_\beta = D_\beta/\alpha$) to describe the influence of open ocean forcing on shelf circulation, which is determined by the ratio of long-wave-limit planetary to TRW speeds (D_β) and linear Ekman number (α). In this study, $Pe_\beta < 1$, which indicates shelf currents decayed rapidly toward the coast. Their results confirm that the ATWs predict the coastal dynamic topography over the continental shelf of the SCS well.

6 Summary

Using sea level data derived from the tide-gauge stations Kanmen, Xiamen, Shanwei, Hongkong, and Zhapo, this study analyzes statistical features of the CSWs, inter-seasonal and seasonal signals. Meanwhile, along-track SLA data derived from multiple satellite altimeters from 1993 to 2020 are applied to detect the cross-shelf structures of the signals. The major results are summarized as follows.

1) CSWs of periods shorter than 40 d propagate along the coast with a phase speed of about 10 m s^{-1} in the ECS and 8 m s^{-1} in the SCS. The dispersion relation indicates that the waves belong to mode 1 CSWs.

2) Owing to the fact that the repeat observation period of the satellite altimeters is comparable with that of CSWs, we combine fragments of the numerous repeat observations of the along-track SLA to reconstruct the cross-shelf structure of CSWs. The results show that the maximum amplitudes of CSWs have remarkable seasonal variability, about 0.6 m during July-September, while only 0.2 m during

April-June. The reconstructed cross-shelf structures of CSWs confirm the property of mode 1 CSWs. Moreover, the energy is trapped within the partial continental shelf shallower than 200 m.

3) The inter-seasonal and seasonal signals present as ATWs on the continental shelf. The amplitudes of ATWs have remarkable seasonal variability, ~0.10 m during October-December, twice larger than 0.04 m, 0.05 m, and -0.06 m during January-March, July-September, and April-June, respectively. These results reveal that the local wind stress substantially influences ATWs on the continental shelf.

4) The results derived from the observation data of the along-coast tide-gauge stations combined with cross-shelf tracks of satellite altimeters are interpreted well by the framework of linear wave theory. It implies that the technological approaches developed in this study are suitable for constructing the cross-shelf structures of CSWs and ATWs on the continental shelf.

However, owing to the neglective wind stress and baroclinicity, higher modes of waves are not discussed in this paper. Observations from moorings and numerical models will be used in our future studies to obtain the characteristics of baroclinic coastal trapped waves.

Acknowledgments

This research was funded by the National Key Research and Development Program of China (2022YFC3104805); National Natural Science Foundation of China (42276019, 42176184, 41976200, 41706025); Innovation Team Plan for Universities in Guangdong Province (2019KCXTF021); First-class Discipline Plan of Guangdong Province (080503032101, 231420003); Observation and Research Station for Tropical Ocean Environment in Coastal Water West of Guangdong.

Data Availability Statement

The tide gauge data are available at https://psmsl.org/data/obtaining/. The along-track SLAs are obtained at ftp-access.aviso.altimetry.fr.

Author contributions

JYL were responsible for writing the original draft. Review and editing were conducted by QAZ. Conceptualization was handled by JYL, QAZ and LLX. TH and YX were responsible for data curation. LLX acquired funding.

Competing interests

The contact author has declared that none of the authors has any competing interests.

Disclaimer

Publisher's note: Copernicus Publications remains neutral with regard to jurisdictional claims in published maps and institutional affiliations.

References:

Aydın, M., Beşiktepe, Ş.T., 2022. Mechanism of generation and propagation characteristics of coastal trapped waves in the Black Sea. Ocean Sci. 18, 1081-1091.

Birol, F., Léger, F., Passaro, M., Cazenave, A., Niño, F., Calafat, F.M., Shaw, A., Legeais, J.-F., Gouzenes, Y., Schwatke, C., Benveniste, J., 2021. The X-TRACK/ALES multi-mission processing system: New advances in altimetry towards the coast. Adv. Space Res. 67, 2398-2415.

Castro, B.M., Lee, T.N., 1995. Wind-forced sea level variability on the southeast Brazilian shelf. Journal of Geophysical Research: Oceans 100, 16045-16056.

Cazenave, A., Moreira, L., 2022. Contemporary sea-level changes from global to local scales: a review. Proceedings of the Royal Society A: Mathematical, Physical and Engineering Sciences 478, 20220049.

Chapman, D.C., 1987. Application of wind-forced, long, coastal-trapped wave theory along the California coast. Journal of Geophysical Research: Oceans 92, 1798-1816.

Chen, D., Su, J., 1987. Continental shelf waves along the coasts of China. Acta Ocean. Sin. 3, 317-334.

Chen, J., Zhu, X.-H., Zheng, H., Nakamura, H., Zhao, R., Wang, M., Park, J.-H., Nishina, A., 2022. Observation of Topographic Rossby Waves Triggered by Kuroshio Path Meander in the East China Sea. Journal of Geophysical Research: Oceans 127, e2022JC018667.

Chen, N., Han, G., Yang, J., Chen, D., 2014. Hurricane Sandy storm surges observed by HY-2A satellite altimetry and tide gauges. Journal of Geophysical Research: Oceans 119, 4542-4548.

Cheng, X., Qi, Y., 2007. Trends of sea level variations in the South China Sea from merged altimetry data. Global and Planetary Change 57, 371-382.

Clarke, A.J., 1977. Observational and Numerical Evidence for Wind-Forced Coastal Trapped Long Waves. J. Phys. Oceanogr. 7, 231-247.

Clarke, A.J., Brink, K., 1985. The response of stratified, frictional flow of shelf and slope waters to fluctuating large-scale, low-frequency wind forcing. J. Phys. Oceanogr. 15, 439-453.

Csanady, G.T., 1978. The Arrested Topographic Wave. J. Phys. Oceanogr. 8, 47-62.

Ding, Y., Bao, X., Shi, M., 2012. Characteristics of coastal trapped waves along the northern coast of the

South China Sea during year 1990. Ocean Dyn. 62, 1259-1285.

Ding, Y., Bao, X., Yao, Z., Song, D., Song, J., Gao, J., Li, J., 2018. Effect of coastal-trapped waves on the synoptic variations of the Yellow Sea Warm Current during winter. Cont. Shelf Res. 167, 14-31.

Ding, Y., Yao, Z., Zhou, L., Bao, M., Zang, Z., 2020. Numerical modeling of the seasonal circulation in the coastal ocean of the Northern South China Sea. Frontiers of Earth Science 14, 90-109.

Dukhovskoy, D., Morey, S., 2011. Simulation of the Hurricane Dennis storm surge and considerations for vertical resolution. Nat. Hazards 58, 511-540.

Fang, G., Chen, H., Wei, Z., Wang, Y., Wang, X., Li, C., 2006. Trends and interannual variability of the South China Sea surface winds, surface height, and surface temperature in the recent decade. Journal of Geophysical Research: Oceans 111.

Gan, J., Li, H., Curchitser, E.N., Haidvogel, D.B., 2006. Modeling South China Sea circulation: Response to seasonal forcing regimes. Journal of Geophysical Research: Oceans 111.

Han, G., Ma, Z., Chen, D., deYoung, B., Chen, N., 2012. Observing storm surges from space: Hurricane Igor off Newfoundland. Sci. Rep. 2.

Heaps, N.S., Huthnance, J.M., Jones, J.E., Wolf, J., 1988. Modelling of storm-driven shelf waves north of Scotland—I. Idealized models. Cont. Shelf Res. 8, 1187-1210.

Ho, C.-R., Zheng, Q., Soong, Y.S., Kuo, N.-J., Hu, J.-H., 2000. Seasonal variability of sea surface height in the South China Sea observed with TOPEX/Poseidon altimeter data. Journal of Geophysical Research: Oceans 105, 13981-13990.

Hormazabal, S., Shaffer, G., Letelier, J., Ulloa, O., 2001. Local and remote forcing of sea surface temperature in the coastal upwelling system off Chile. Journal of Geophysical Research: Oceans 106, 16657-16671.

Hsueh, Y., Pang, I.-C., 1989. Coastally Trapped Long Waves in the Yellow Sea. J. Phys. Oceanogr. 19, 612-625.

Hsueh, Y., Romea, R.D., 1983. Wintertime winds and coastal sea-level fluctuations in the Northeast China Sea. Part I: observations. J. Phys. Oceanogr. 13, 2091-2106.

Huang, D., Zeng, D., Ni, X., Zhang, T., Xuan, J., Zhou, F., Li, J., He, S., 2015. Alongshore and cross-shore circulations and their response to winter monsoon in the western East China Sea. Deep Sea Res. Part II.

Kajikawa, Y., Yasunari, T., 2005. Interannual variability of the 10–25- and 30–60-day variation over the South China Sea during boreal summer. Geophysical Research Letters 32.

Li, J., Li, M., Wang, C., Zheng, Q., Xu, Y., Zhang, T., Xie, L., 2023a. Multiple mechanisms for chlorophyll a concentration variations in coastal upwelling regions: a case study east of Hainan Island in the South China Sea. Ocean Sci. 19, 469-484.

Li, J., Zheng, Q., Hu, J., Fan, Z., Zhu, J., Chen, T., Zhu, B., Xu, Y., 2015. Wavelet analysis of coastal-trapped waves along the China coast generated by winter storms in 2008. Acta Ocean. Sin. 34 22-31.

Li, J., Zheng, Q., Hu, J., Xie, L., Zhu, J., Fan, Z., 2016. A case study of winter storm-induced continental shelf waves in the northern South China Sea in winter 2009. Cont. Shelf Res. 125, 127-135.

Li, J., Zheng, Q., Li, M., Li, Q., Xie, L., 2021. Spatiotemporal Distributions of Ocean Color Elements in Response to Tropical Cyclone: A Case Study of Typhoon Mangkhut (2018) Past over the Northern South China Sea. Remote Sensing 13, 687.

Li, J., Zhou, C., Li, M., Zheng, Q., Li, M., Xie, L., 2023b. A case study of continental shelf waves in the northwestern South China Sea. Acta Ocean. Sin.

Li, L., 1993. A study of winter subtidal sea level fluctuation along the northern coast of the South China

676   Sea. Tropic Oceanology.

677   Lin, W., Lin, H., Hu, J., 2021. The Tilt of Mean Dynamic Topography and its Seasonality Along the Coast

678   of the Chinese Mainland. Journal of Geophysical Research: Oceans 126, e2020JC016778.

679   Lin, W., Lin, H., Hu, J., Huang, L., 2022. Relative Contributions of Open-Ocean Forcing and Local Wind

680   to Sea Level Variability Along the West Coasts of Ocean Basins. Journal of Geophysical Research:

681   Oceans 127, e2022JC019218.

682   Lin, X., Yang, J., 2011. An asymmetric upwind flow, Yellow Sea Warm Current: 2. Arrested topographic

683   waves in response to the northwesterly wind. Journal of Geophysical Research: Oceans 116.

684   Lin, X., Yang, J., Guo, J., Zhang, Z., Yin, Y., Song, X., Zhang, X., 2011. An asymmetric upwind flow,

685   Yellow Sea Warm Current: 1. New observations in the western Yellow Sea. Journal of Geophysical

686   Research: Oceans 116.

687   Marshall, A.G., Hendon, H.H., 2013. Impacts of the MJO in the Indian Ocean and on the Western

688   Australian coast. Clim. Dyn., 1-17.

689   Morey, S.L., Baig, S., Bourassa, M.A., Dukhovskoy, D.S., O'Brien, J.J., 2006. Remote forcing

690   contribution to storm-induced sea level rise during Hurricane Dennis. Geophys. Res. Lett. 33.

691   Mysak, L.A., 1980. Topographically trapped waves. Annual Review of Fluid Mechanics 12, 45-76.

692   Quan, Q., Cai, Z., Jin, G., Liu, Z., 2021. Topographic Rossby Waves in the Abyssal South China Sea. J.

693   Phys. Oceanogr. 51, 1795-1812.

694   Robinson, A., 1964. Continental shelf waves and the response of sea level to weather systems. J. Geophys.

695   Res. 69, 367-368.

696   Schulz, W.J., Mied, R.P., Snow, C.M., 2011. Continental shelf wave propagation in the Mid-Atlantic

697   Bight: a general dispersion relation. J. Phys. Oceanogr. 42, 558-568.

698   Shen, J., Zhang, S., Zhang, J., Zeng, M., Fang, W., 2021. Observation of continental shelf wave

699   propagating along the eastern Taiwan Strait during Typhoon Meranti 2016. Journal of Oceanology and

700   Limnology 39, 45-55.

701   Thiebaut, S., Vennell, R., 2010. Observation of a fast continental shelf wave generated by a storm

702   impacting Newfoundland using wavelet and cross-wavelet analyses. J. Phys. Oceanogr. 40, 417-428.

703   Vialard, J., Shenoi, S., McCreary, J., Shankar, D., Durand, F., Fernando, V., Shetye, S., 2009.

704   Intraseasonal response of the northern Indian Ocean coastal waveguide to the Madden-Julian Oscillation.

705   Geophys. Res. Lett. 36.

706   Vignudelli, S., Birol, F., Benveniste, J., Fu, L.-L., Picot, N., Raynal, M., Roinard, H., 2019. Satellite

707   Altimetry Measurements of Sea Level in the Coastal Zone. Surv. Geophys. 40, 1319-1349.

708   Wang, B., Huang, F., Wu, Z., Yang, J., Fu, X., Kikuchi, K., 2009. Multi-scale climate variability of the

709   South China Sea monsoon: A review. Dyn. Atmos. Oceans 47, 15-37.

710   Wang, D.-P., Mooers, C.N., 1976. Coastal-trapped waves in a continuously stratified ocean. J. Phys.

711   Oceanogr. 6, 853-863.

712   Wu, H., 2021. Beta-Plane Arrested Topographic Wave as a Linkage of Open Ocean Forcing and Mean

713   Shelf Circulation. J. Phys. Oceanogr. 51, 879-893.

714   Xie, L., Zheng, Q., Zhang, S., Hu, J., Li, M., Li, J., Xu, Y., 2018. The Rossby normal modes in the South

715   China Sea deep basin evidenced by satellite altimetry. International Journal of Remote Sensing 39, 399-

716   417.

717   Xu, Y., Lin, M., Zheng, Q.a., Song, Q., Ye, X., 2016. A study of sea level variability and its long-term

718   trend in the South China Sea. Acta Oceanologica Sinica 35, 22-33.

719   Yin, L., Qiao, F., Zheng, Q., 2014. Coastal-trapped waves in the East China Sea observed by a mooring

array in winter 2006. J. Phys. Oceanogr. 44, 576-590.

Zhao, R., Zhu, X.-H., Park, J.-H., 2017. Near 5-Day Nonisostatic Response to Atmospheric Surface Pressure and Coastal-Trapped Waves Observed in the Northern South China Sea. J. Phys. Oceanogr. 47, 2291-2303.

Zheng, Q., Hu, J., Zhu, B., Feng, Y., Jo, Y.-H., Sun, Z., Zhu, J., Lin, H., Li, J., Xu, Y., 2014. Standing wave modes observed in the South China Sea deep basin. Journal of Geophysical Research: Oceans 119, 4185-4199.

Zheng, Q., Zhu, B., Li, J., Sun, Z., Xu, Y., Hu, J., 2015. Growth and dissipation of typhoon-forced solitary continental shelf waves in the northern South China Sea. Clim. Dyn. 45, 853-865.

Zhou, C., Li, J., Zheng, Q., Xie, L., 2023. Characteristics of winter continental shelf waves in the northern South China Sea. Journal of Guangdong Ocean University 43, 89-97.

Zhuang, W., Xie, S.P., Wang, D.X., Taguchi, B., Aiki, H., Sasaki, H., 2010. Intraseasonal variability in sea surface height over the South China Sea. Journal of Geophysical Research-Oceans 115.